PHYSICAL REVIEW B **69**, 205105 (2004)

Electronic structure of the transition-metal dicyanamides $M[\mathrm{N(CN)}_2]_2$ (M=Mn,Fe,Co,Ni,Cu)

D. O. Demchenko and Amy Y. Liu
Department of Physics, Georgetown University, Washington, DC 20057, USA

E. Z. Kurmaev, L. D. Finkelstein, and V. R. Galakhov
Institute of Metal Physics, Russian Academy of Sciences, Ural Division, 620219 Yekaterinburg GSP-170, Russia

A. Moewes
Department of Physics and Engineering Physics, University of Saskatchewan, 116 Science Place, Saskatoon, Saskatchewan S7N 5E2, Canada

S. G. Chiuzbăian* and M. Neumann
Universität Osnabrück, Fachbereich Physik, D-49069 Osnabrück, Germany

Carmen R. Kmety
Advanced Photon Source, Argonne National Laboratory, Argonne, Illinois 60439, USA

Kenneth L. Stevenson
Department of Chemistry, Indiana University Purdue University, Fort Wayne, Indiana 46805, USA

(Received 12 November 2003; published 20 May 2004)

The electronic structure of $M[\mathrm{N(CN)}_2]_2$ (M=Mn,Fe,Co,Ni,Cu) molecular magnets has been investigated using x-ray emission spectroscopy and x-ray photoelectron spectroscopy as well as theoretical density-functional-based methods. Both theory and experiments show that the top of the valence band is dominated by M $3d$ bands, while a strong hybridization between C $2p$ and N $2p$ states determines the valence-band electronic structure away from the top. The $2p$ contributions from nonequivalent nitrogen sites have been identified using resonant inelastic x-ray scattering spectroscopy with the excitation energy tuned near the N $1s$ threshold. The binding energy of the M $3d$ bands and the hybridization between N $2p$ and M $3d$ states both increase when going across the row from M=Mn to M=Cu. Localization of the Cu $3d$ states also leads to weak screening of Cu $2p$ and $3s$ states, which accounts for shifts in the core $2p$ and $3s$ spectra of the transition-metal atoms. Calculations indicate that the ground-state magnetic ordering, which varies across the series, is largely dependent on the occupation of the metal $3d$ shell and that structural differences in the superexchange pathways for different compounds play a secondary role.

DOI: 10.1103/PhysRevB.69.205105 PACS number(s): 75.50.Xx, 71.20.Rv, 71.70.−d, 75.30.Et

I. INTRODUCTION

Molecule-based magnets have been a subject of interest in the past decade, after the discovery of room-temperature magnetic ordering in some of these materials.[1,2] Interest is driven not only by the potential for use in applications such as information storage and processing, but also by fundamental questions about the origin of magnetic ordering in these materials. The transition-metal dicyanamides, $M[\mathrm{N(CN)}_2]_2$ where M is a $3d$ transition metal, provide an example where, even within an isostructural series of compounds, the magnetic ordering can differ substantially depending on the metal species and details of the crystal structure. Experimental studies of the structural and magnetic properties of the dicyanamides with M=Mn, Fe, Co, Ni, and Cu have been performed by several groups.[3–8] $\mathrm{Mn[N(CN)_2]_2}$ and $\mathrm{Fe[N(CN)_2]_2}$ have been found to be canted antiferromagnets, while $\mathrm{Co[N(CN)_2]_2}$ and $\mathrm{Ni[N(CN)_2]_2}$ have been found to be ferromagnets. $\mathrm{Cu[N(CN)_2]_2}$ has been reported to be paramagnetic, at least down to a few kelvins, and a recent experiment has found that it becomes a ferromagnet below 1.8 K.[8] Thus the compounds with transition-metal ions having six or fewer $3d$ electrons order as canted antiferromagnets, while those with seven or more $3d$ electrons order as ferromagnets. The Curie (or Néel) temperatures of these materials range from 1.8 K for $\mathrm{Cu[N(CN)_2]_2}$ to 22.7 K for $\mathrm{Ni[N(CN)_2]_2}$. $\mathrm{Ni[N(CN)_2]_2}$ and $\mathrm{Fe[N(CN)_2]_2}$ have been found to have the largest coercive fields of all known metal-organic magnets—7975 and 17 800 Oe, respectively.

The molecular building block of the bulk dicyanamides consists of a divalent metal ion that is twofold coordinated by two $\mathrm{N(CN)_2}$ groups. When the molecular units pack to form the bulk crystal, the negatively charged CN groups at the end of neighboring molecules interact with the positive central metal ion in such a way that the metal ion becomes surrounded by an octahedron of six N atoms. The local symmetry around the metal site is tetragonal, with the original molecular axis corresponding to the long axis. The primitive cell contains two formula units with their long axes rotated in opposite directions in the xy plane, leading to an orthorhombic cell. The metal ions are the source of magnetic moments while the organic species provide superexchange pathways between the magnetic centers.

In this paper we report a combined experimental and theoretical study of the electronic structure of $M[\mathrm{N(CN)}_2]_2$ with $M=$Mn, Fe, Co, Ni, Cu. We have measured x-ray emission spectra (XES) and x-ray photoemission spectra (XPS) across the series. Generally, XPS probes the total occupied density of states (DOS) whereas XES probes the site-selective partial DOS due to the dipole selection rules. In the case of carbon and nitrogen $K\alpha$ XES, which correspond to $2p\rightarrow 1s$ transitions, the occupied $2p$ states can be studied. Similarly, $M\,L\alpha,\beta$ XES, related to the $3d4s\rightarrow 2p$ transition, gives information about occupied $3d$ bands. The comparison of XPS and XES in the binding-energy scale yields information about the distribution of the partial and total DOS in multicomponent systems. The measured spectra are compared with results of density-functional calculations. In a recent paper focusing on the electronic structure of $\mathrm{Mn}[\mathrm{N(CN)}_2]_2$, reasonable agreement was found between theory and experiment for the electronic structure, magnetic ordering, and magnetic anisotropy.[9] Here we find that the direct comparison of density-functional calculations with experimental data is not as straightforward for some of the other compounds in the series.

II. EXPERIMENTAL AND CALCULATION DETAILS

The x-ray fluorescence measurements were performed at Beamline 8.0 at the Advanced Light Source (ALS) of Lawrence Berkeley National Laboratory (LBNL). Carbon and nitrogen $K\alpha$ ($2p\rightarrow 1s$ transition) and $M\,L\alpha,\beta$ ($3d4s\rightarrow 2p$ transition) x-ray emission spectra were taken, employing the University of Tennessee at Knoxville soft x-ray fluorescence endstation.[10] Photons with energy of 300 eV above the carbon K edge were delivered to the endstation via the beamline's 89-period, 5 cm undulator insertion device and spherical monochromator. For nitrogen $K\alpha$ and $M\,L\alpha,\beta$ XES, an excitation-energy dependence was measured near the N $1s$ and M $2p$ thresholds. The carbon and nitrogen $K\alpha$ spectra were obtained with an energy resolution of 0.3–0.4 eV. The $M\,L\alpha,\beta$ XES were measured with an energy resolution of 0.7–0.8 eV.

The XPS measurements were performed with an electron spectroscopy for chemical analysis spectrometer of Physical Electronics (PHI 5600 ci) with monochromatized Al $K\alpha$ radiation of a 0.3 eV full width at half maximum. The energy resolution of the analyzer was 1.5% of the pass energy. The pressure in the vacuum chamber during the measurements was below 5×10^{-9} mbar. Prior to XPS measurements, the samples were fractured in ultrahigh vacuum. All photoemission studies were performed at room temperature on freshly cleaved surfaces. Charging of the insulating $M[\mathrm{N(CN)}_2]_2$ samples was compensated with an electron gun. Because there is no saturated carbon in these molecules, the binding energies cannot be corrected using the C $1s$ line. Therefore we have used an alternative way[11] of fixing the N $1s$ line of the cyanide group at 399.6 eV.

Polycrystalline pressed pellets of $M[\mathrm{N(CN)}_2]_2$ compounds were used for XES and XPS measurements. Details about the sample preparation can be found in Refs. 6 and 7.

TABLE I. Calculated total-energy differences between different spin configurations (in eV/M site), local spin magnetic moments (in μ_B), and band gaps (in eV). For $M=$Mn and Fe, the calculated spin moments and gaps are given for the antiferromagnetic state, while for $M=$Co, Ni, and Cu, results for the ferromagnetic state are presented. Experimental moments from neutron powder diffraction experiments reported in Refs. 6, 7, and 26 are shown for comparison and include both spin and orbital contributions. Estimates for band gaps obtained from diffuse reflectance spectroscopy on powder samples at room temperature are also included.

	ΔE		μ_M		E_g	
	NM-AF	AF-FM	calc.	expt.	calc.	expt.
$\mathrm{Mn}[\mathrm{N(CN)}_2]_2$	2.490	-0.018	4.50	4.61	2.12	2.07
$\mathrm{Fe}[\mathrm{N(CN)}_2]_2$	0.862	0.025	3.59	4.53	0.00[a]	1.46
$\mathrm{Co}[\mathrm{N(CN)}_2]_2$	0.735	0.023	2.54	2.67	0.24	2.40
$\mathrm{Ni}[\mathrm{N(CN)}_2]_2$	0.939	0.015	1.59	2.21	1.36	1.97
$\mathrm{Cu}[\mathrm{N(CN)}_2]_2$	0.287	0.000	0.65	1.05	0.52	1.91

[a] Calculations yield metallic state for AF $\mathrm{Fe}[\mathrm{N(CN)}_2]_2$ (see text).

Diffuse reflectance spectroscopy was used to measure the lowest electronic transition observable in the visible region, which can be interpreted as possible band gap energies. The reflectance spectra were taken on powdered samples at room temperature in a 1 mm quartz cuvette which was illuminated by light from a 75 W Xe high-pressure arc lamp. The reflected light was admitted into an Acton Spectropro 300i 300 mm spectrometer with a Hammamatsu charge-coupled device detector, which gave light intensities versus wavelength from 300 to 800 nm. The spectrum of a ''white'' standard, consisting of powdered NaCl, was used to determine the absorbance, $\log(I_0/I_s)$, as a function of wavelength for each sample, where I_0 is the intensity of the white standard and I_s is the intensity of the sample compound.

For comparison with the experimental results, electronic-structure calculations were performed for ferromagnetic (FM), antiferromagnetic (AF), and nonmagnetic (NM) phases using the crystal structures determined from x-ray- and neutron-diffraction experiments.[3,5–8] Spins were restricted to be collinear. Calculations were carried out using the VASP program,[12] a density-functional-based code employing plane-wave basis sets and ultrasoft pseudopotentials. The electron-electron interaction was treated in the generalized gradient approximation (GGA),[13,14] and electronic wave functions were expanded in plane waves up to a kinetic energy cutoff of 435 eV. Monkhorst-Pack meshes[15] of up to $8\times 8\times 8$ **k**-points were used to sample the Brillouin zone, and the linear tetrahedron method was used to integrate over the Brillouin zone.

III. MAGNETIC PROPERTIES

Table I summarizes the results of the total-energy calculations. Density-functional-theory (DFT) calculations for terminated cluster models yield similar results.[16] Experimentally, $\mathrm{Mn}[\mathrm{N(CN)}_2]_2$ and $\mathrm{Fe}[\mathrm{N(CN)}_2]_2$ are both canted antiferromagnets. In the Mn compound, the canting angle is reported to be at most a few degrees,[6] while in the Fe compound, the canting angle is estimated to be 20°–23°.[8] Our calculations find $\mathrm{Mn[N(CN)_2]_2}$ to be antiferromagnetic, but neglect of both the canting and spin-orbit interaction in $\mathrm{Fe[N(CN)_2]_2}$ results in the FM phase being favored. Similar results were recently obtained in Ref. 17. We expect that when spins are not restricted to be collinear, density-functional theory would yield an AF ground state for $\mathrm{Fe[N(CN)_2]_2}$. For $\mathrm{Ni[N(CN)_2]_2}$ and $\mathrm{Co[N(CN)_2]_2}$, we find the ground state to be ferromagnetic, in agreement with experiments. In the case of $\mathrm{Cu[N(CN)_2]_2}$, the FM and AF phases are calculated to be very close in energy and favored over the NM phase. Magnetization studies show no long-range ordering above 2 K,[5] but a recent study[8] finds that $\mathrm{Cu[N(CN)_2]_2}$ becomes ferromagnetic at lower temperatures with $T_c \sim 1.8$ K. Hence we report results of our calculations for the FM phase.

In superexchange systems, the magnitude and sign of the one-electron contribution to the exchange interaction depend on the filling of those orbitals on neighboring magnetic centers that interact via a bridging ligand.[18–20] The relevant orbitals, i.e., those with nonzero interaction matrix elements, depend in turn on the geometry of the superexchange pathway. The magnetic ordering is thus determined by an interplay between the occupation of the d shell and the superexchange angle. In $M\mathrm{[N(CN)_2]_2}$, neighboring M sites are connected through a M-[N-C-N]-M pathway, where the two N sites along the path are inequivalent. The M-[N-C-N]-M angle increases monotonically when going from $\mathrm{Mn[N(CN)_2]_2}$ to $\mathrm{Ni[N(CN)_2]_2}$, with a total change of about 2.5°.[6] It has been suggested that this structural change in the pathway is responsible for the different magnetic ground states in the dicyanamides, with the angle passing through a critical value in going across the $3d$ series.[6] Our calculations find that such small changes in structure do not change the energetic ordering of the magnetic phases. The occupation of the $3d$ shell is evidently a more significant factor in determining the sign of the superexchange interaction in these systems.

Density-functional theory typically underestimates magnetic moments, but, as shown in Table I, discrepancies for $M=$Fe and Ni appear unusually large. This is likely because the measured magnetic moments in the table, determined from neutron powder diffraction studies,[6,8] include both spin and orbital contributions. For octahedrally coordinated M^{2+} cations without spin-orbit coupling, the orbital moment is expected to be completely quenched for $M=$Mn, Ni, and Cu, and unquenched or partially quenched for $M=$Fe and Co.[21] With spin-orbit coupling, the quenching due to the crystal field is incomplete, resulting in a Landé g-factor that can deviate from 2.[7,8] With no mechanism for unquenching the orbital moment within our calculations, a direct comparison between the theoretical and experimental moments in Table I is not appropriate.

It is well known that the local spin magnetic moment is related to spectral splitting of the $3s$ core-level x-ray photoemission spectra in transition metals and their compounds. The splitting originates from the exchange coupling between the $3s$ hole and the $3d$ electrons and the magnitude of the splitting is proportional to $(2S+1)$, where S is the local spin of the $3d$ electrons in the ground state.[22] In addition to the exchange interaction the charge-transfer process has to be taken into account. The $3s$ spectra of the $M\mathrm{[N(CN)_2]_2}$ materials together with those of simple oxides MnO, FeO, CoO, NiO, and CuO are shown in Fig. 1.

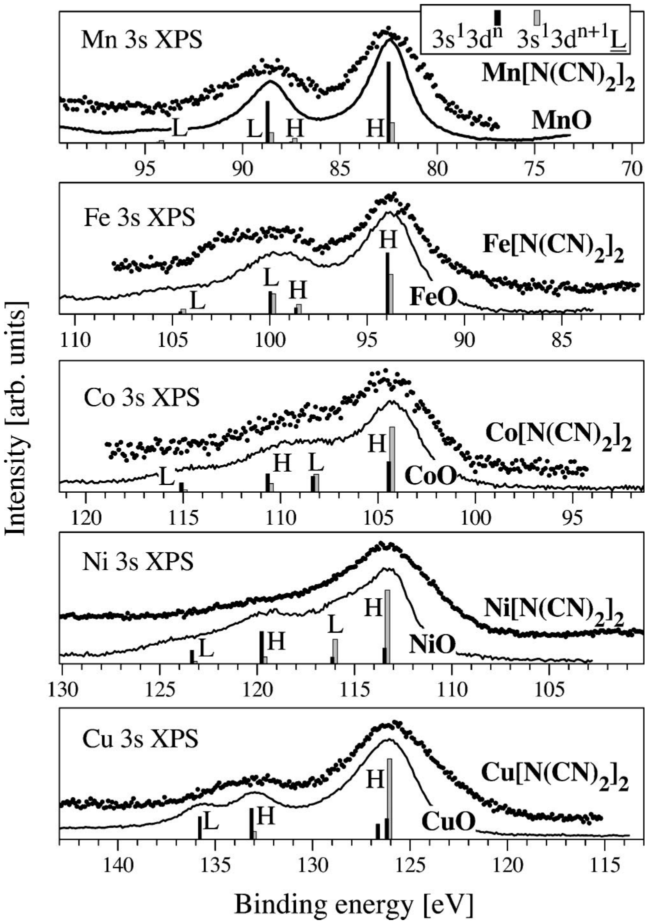

FIG. 1. M $3s$ x-ray photoelectron spectra of $M\mathrm{[N(CN)_2]_2}$ (points) and simple oxides MO (thick lines). The maxima of the M $3s$ spectra of monoxides have been shifted in binding energy to facilitate comparison with the $M\mathrm{[N(CN)_2]_2}$ spectra. The contributions of the $3s^13d^n$ and $3s^13d^{n+1}L$ final state configurations are shown, with high-spin and low-spin states labeled by "H" and "L" respectively.

For the simple oxides, the contributions of the $3s^13d^n$ (vertical black lines) and $3s^13d^{n+1}\underline{L}$ (vertical gray lines) final-state configurations are shown. Here, $\underline{L}$ denotes an electronic hole in ligand $2p$ state due to the charge-transfer process. "L" and "H" in Fig. 1 denote high-spin and low-spin states, respectively. The method of calculation of different contributions to the spectra is described elsewhere.[23,24]

The Mn $3s$ spectrum shows two main peaks, formed mainly by $3s^13d^5$ final states. The magnitude of the exchange splitting for $\mathrm{Mn[N(CN)_2]_2}$, 6.5 eV, is very similar to that in MnO, 6.2 eV (with a local magnetic moment of 4.6 μ_B),[25] which indicates the Mn $3d^5$ ground-state configuration for $\mathrm{Mn[N(CN)_2]_2}$. This correlates well with calculated and measured spin moments of $\mathrm{Mn[N(CN)_2]_2}$ pre-

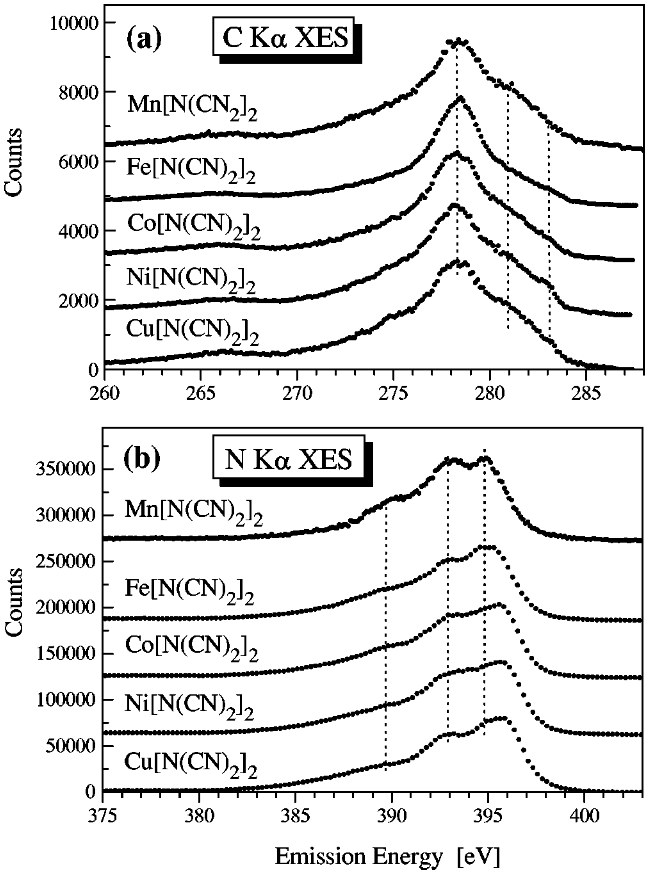

FIG. 2. Nonresonant (a) carbon and (b) nitrogen $K\alpha$ XES of $M[\mathrm{N(CN)_2}]_2$ compounds.

sented in Table I. The M $3s$ spectra of $\mathrm{Ni[N(CN)_2]_2}$, $\mathrm{Co[N(CN)_2]_2}$, and $\mathrm{Fe[N(CN)_2]_2}$ show a complex structure formed by both $3s^1 3d^n$ and $3s^1 3d^{n+1}\underline{L}$ final-state configurations. Coexistence of both exchange and charge-transfer effects makes the comparison of the M $3s$ splitting with the local magnetic moments difficult. Similarities with the spectra of the monoxides suggest that the M $3s$ energy splitting is systematically reduced with increasing M atomic number, as expected for transition-metal ions with nominal 2^+ valence (Table I). For $\mathrm{Cu[N(CN)_2]_2}$, the exchange splitting is expected for the $3s^1 3d^9$ configuration only, which is localized in the energy interval from 130 to 135 eV. Low-energy resolution limits our ability to separate this splitting in the present data, but it has been observed in copper oxides (see Fig. 1 and Ref. 24).

IV. ELECTRONIC STRUCTURE

Figure 2 shows the measured nonresonant carbon and nitrogen $K\alpha$ XES of the $M[\mathrm{N(CN)_2}]_2$ compounds. As seen, the carbon $K\alpha$ XES [Fig. 2(a)] are very similar across the series because of the same local atomic and electronic structure of carbon atoms in cyano groups. On the other hand, the nitrogen atoms occupy two nonequivalent sites in the crystal structure of $M[\mathrm{N(CN)_2}]_2$ compounds, where each M atom has two N(1) neighbors along the long axis and four N(2) neighbors from CN anions along the other axes.[6] The nitrogen $K\alpha$ XES of $M[\mathrm{N(CN)_2}]_2$ [Fig. 2(b)] has contributions from both sites. The N $K\alpha$ spectrum of the reference compound $\mathrm{Na_4Fe(CN)_6(OH_2O)}$ [Fig. 3(a)] shows N contributions from cyano groups and is quite different from the nonresonant nitrogen spectra of $M[\mathrm{N(CN)_2}]_2$. In our XPS measurements, the N $1s$ spectrum is split into two main lines separated by approximately 1.6 eV, corresponding to the difference in the N $1s$ binding energies of the two nonequivalent N sites (Table II).

Additional measurements were made for resonantly excited nitrogen $K\alpha$ XES in $\mathrm{Mn[N(CN)_2]_2}$. The energy dependence of the spectra when the excitation energy was tuned near the N $1s$ threshold is shown in Fig. 3(a). The intensities of the peaks at 389.9, 392.7, and 394.8 eV change with excitation energy. The nonresonant spectrum d excited far from the N $1s$ threshold can be described as a superposition of spectra b and c [Fig. 3(b)], corresponding to contributions from selectively excited nonequivalent nitrogen atoms. Based on our measurements of the nonresonant N $K\alpha$ XES of $\mathrm{Na_4Fe(CN)_6(OH_2O)}$ [Fig. 2(b)], we can attribute the origin of the resonant spectrum of $\mathrm{Mn[N(CN)_2]_2}$ excited near peaks a and b of the N $1s$ total electron yield (TEY) to N(2) atoms located in cyano groups, whereas the spectrum excited near peak c of the N $1s$ TEY can be explained by contributions from both N(1) and N(2) atoms.

The valence band (VB) XPS and the XES of the constituents of $M[\mathrm{N(CN)_2}]_2$ are compared in Figs. 4–8. We have selected for this comparison the nonresonant carbon and nitrogen $K\alpha$ XES shown in Fig. 2 and the M $L\alpha$ XES ($3d4s \rightarrow 2p_{3/2}$ transition) which were excited just above the $L\alpha$ threshold to exclude the excitation of the M $L\beta$ XES ($3d4s \rightarrow 2p_{1/2}$ transition) that overlaps the M $L\alpha$ XES due to spin-orbit splitting. To convert the XES of the constituents to the binding-energy scale, we have subtracted emission energies from the XPS binding energies of core levels (Table II). According to this comparison, the top of the valence band (a) is derived mainly from M $3d$ and N $2p$ states. Towards the

TABLE II. XPS core level binding energies and location of $3d$-band maxima (in eV) of $M[\mathrm{N(CN)_2}]_2$, with M = Mn,Fe,Co,Ni,Cu.

	$\mathrm{Mn[N(CN)_2]_2}$	$\mathrm{Fe[N(CN)_2]_2}$	$\mathrm{Co[N(CN)_2]_2}$	$\mathrm{Ni[N(CN)_2]_2}$	$\mathrm{Cu[N(CN)_2]_2}$
C $1s$	287.7	287.7	287.1	288.0	288.0
N $1s$	399.6; 398.0	399.6; 398.3	399.6; 398.5	399.6; 397.2	399.6; 397.8
M $2p_{3/2}$	642.4	710.1	782.2	857.2	936.5
M $3d$	4.0	4.1	4.2	4.7	6.0

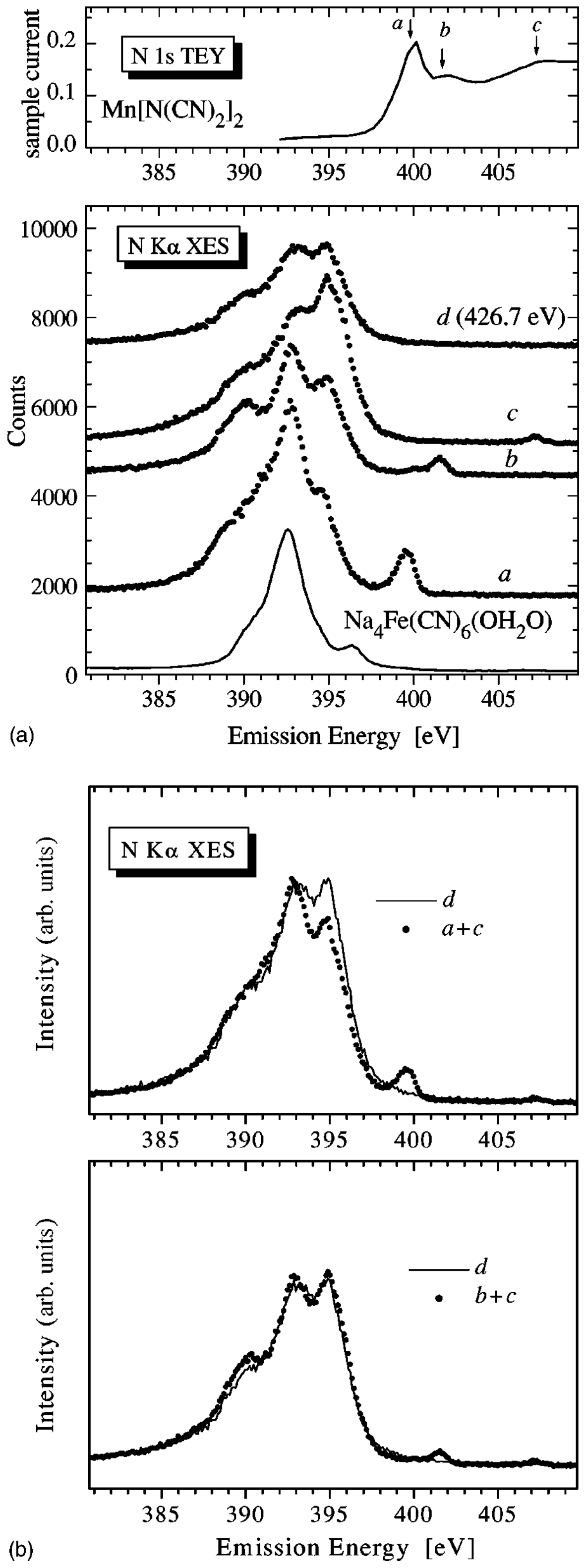

FIG. 3. Resonant N $K\alpha$ XES of Mn$[N(CN)_2]_2$. Spectra obtained with different excitation energies near the N 1s threshold are shown in (a). The N $K\alpha$ XES for the reference compound $Na_4Fe(CN)_6(OH_2O)$ is included for comparison. The nonresonant spectrum d is compared to superpositions of resonant spectra a, b, and c in (b). The nonresonant spectrum is better represented by a superposition of b and c than by a superposition of a and c.

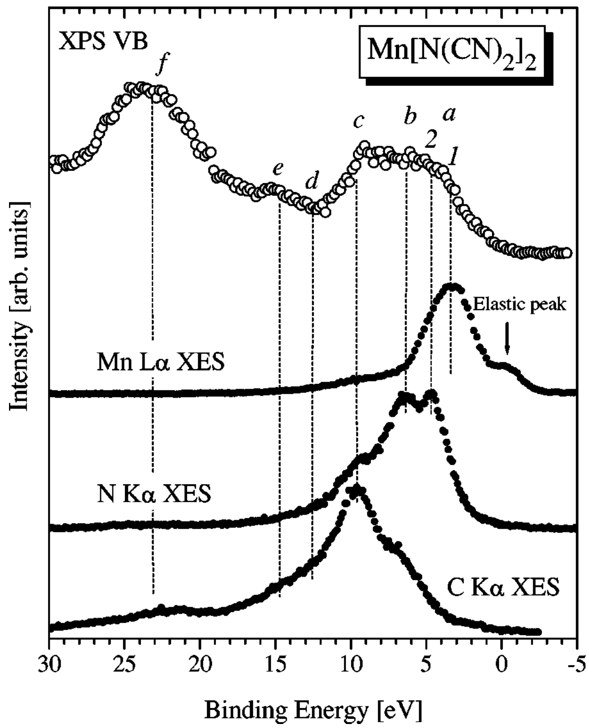

FIG. 4. Comparison of XPS VB and XES of constituents for Mn$[N(CN)_2]_2$ in the binding-energy scale.

middle of the valence band the M 3d, N 2p, and C 2p states are strongly hybridized, forming a broad structure (b–d). At the bottom of the valence band (e) are mixed carbon and nitrogen 2p states. Atomic-like carbon and nitrogen 2s states

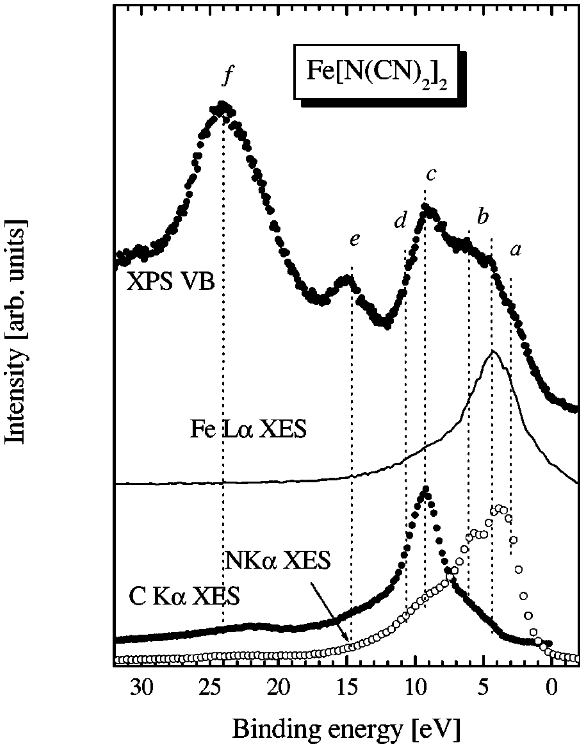

FIG. 5. Comparison of XPS VB and XES of constituents for Fe$[N(CN)_2]_2$ in the binding-energy scale.

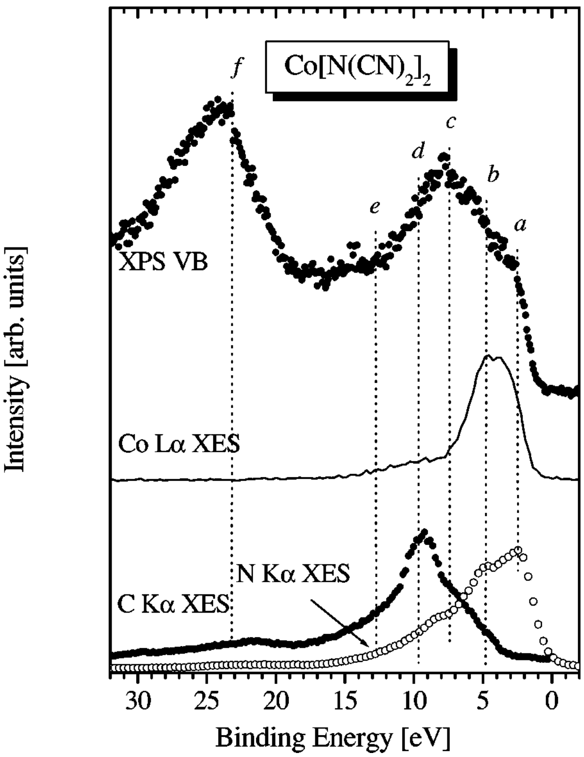

FIG. 6. Comparison of XPS VB and XES of constituents for $Co[N(CN)_2]_2$ in the binding-energy scale.

are located in region (f), with binding energy around 20–25 eV.

For comparison, we present theoretical results for $Ni[N(CN)_2]_2$ as an example. The calculated electronic DOS of $Ni[N(CN)_2]_2$ is shown in Fig. 9. The total DOS is in the lowest panel, and site- and *l*-projected DOS are plotted in the other panels. In the lowest panel, a Gaussian broadening of 1.0 eV has been introduced to simulate the effect of finite instrumental resolution. The partial DOS in the upper three panels have been broadened by 0.2 eV to help in identifying features seen in the experimental XES spectra. Features in the DOS are labeled (a)–(f) as in the experimental XPS spectra. The nature of the states at different energies is generally consistent with what is found in the XPS/XES comparison. Regions (a) and (b) near the top of the valence band are dominated by Ni $3d$ states, with some hybridization with C and N $2p$ states, and they correspond to the peak in the Ni $L\alpha$ XES spectrum. Regions (c) and (d) contain strong contributions from C $2p$ and N $2p$ states, as seen in the C and N XES spectra, as well as some Ni $3d$ states. Peak (e), approximately 12 eV below the top of the valence band, is primarily of C $2p$ and C $2s$ character, and N $2p$ contributions from N(1) sites. Region (f) has significant contributions from the N $2s$, C $2s$, and C $2p$ states and is observed in the C $K\alpha$ XES spectrum.

For the other compounds, the electronic DOS is very similar to that of $Ni[N(CN)_2]_2$ from about 25 eV below the top of the valence band up to region (d) where $3d$ states of the transition metal start playing a significant role. The hybridization between N $2p$ and M $3d$ states increases with the M atomic number. For $M=$Mn, Fe, and Co, states near the

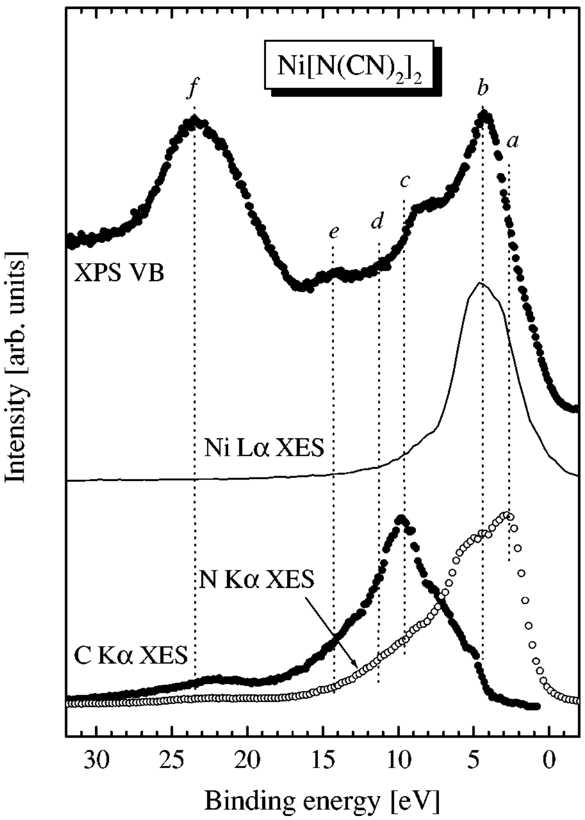

FIG. 7. Comparison of XPS VB and XES of constituents for $Ni[N(CN)_2]_2$ in the binding-energy scale.

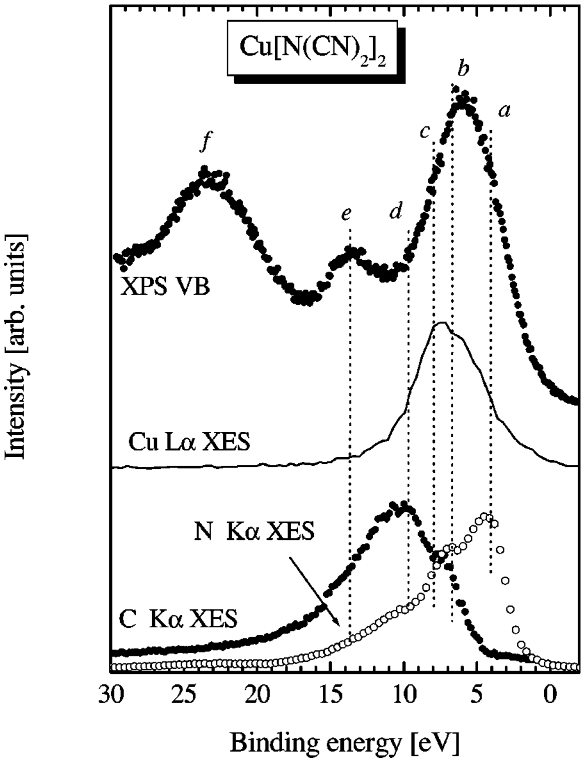

FIG. 8. Comparison of XPS VB and XES of constituents for $Cu[N(CN)_2]_2$ in the binding-energy scale.

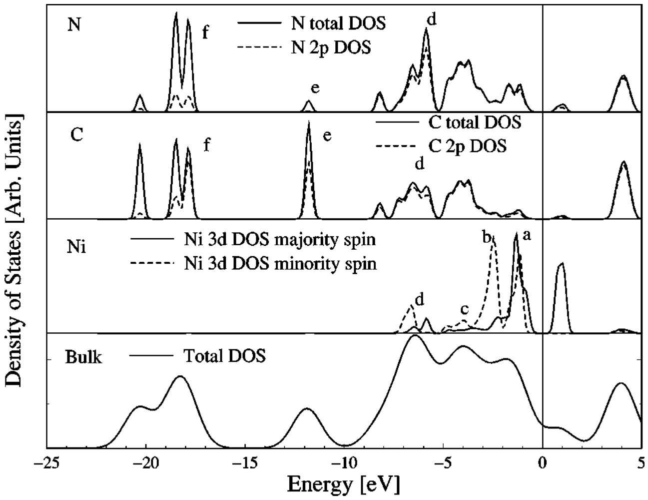

FIG. 9. Total and partial density of states calculated for ferromagnetic Ni$[N(CN)_2]_2$. The total DOS in the bottom panel has been broadened by 1.0 eV, while the site-projected DOS in the top three panels have been broadened by 0.2 eV.

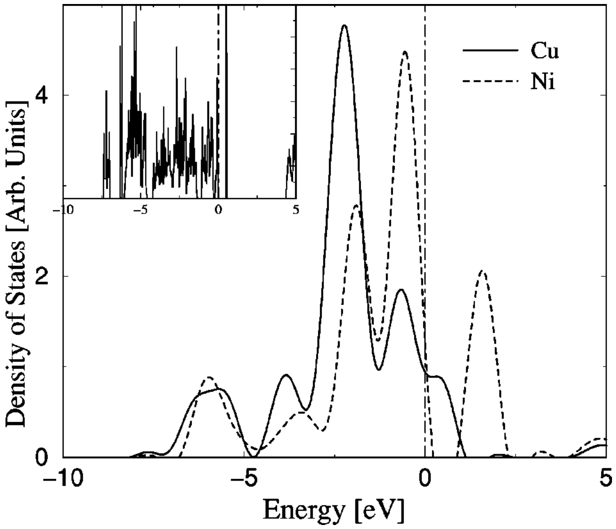

FIG. 10. Cu and Ni d densities of states calculated for FM Cu$[N(CN)_2]_2$ and FM Ni$[N(CN)_2]_2$. To emphasize gross features in the DOS, Methfessel-Paxton (fifth order) smearing of 1 eV is used. The band gaps are masked by this broadening, and the Fermi level is set to 0 eV. The inset shows total FM Cu$[N(CN)_2]_2$ densities of states calculated with the linear tetrahedron method.

top of the valence band are overwhelmingly of M d character, while for $M=$Ni and Cu, the relative contribution of N p states is increased. In both the calculations and the experiments, the weight of the $3d$-derived bands shifts with respect to the top of the valence band. Based on the XPS valence bands, the maximum of the $3d$ bands varies from about 4 eV for Mn$[N(CN)_2]_2$ to about 6 eV for Cu$[N(CN)_2]_2$ (see Figs. 4–8 and Table II). This result is confirmed by the $M\,L\alpha$ XES converted to the binding-energy scale. In addition, in the calculations, we find, for example, about a 1.5 eV difference in the position of the main maxima of the occupied d-DOS weights in Cu$[N(CN)_2]_2$ compared to Ni$[N(CN)_2]_2$ (Fig. 10), which is similar to what is observed experimentally (Table II). The deepening of $3d$ states found for Cu$[N(CN)_2]_2$ is due to the localization of d electrons at the end of the $3d$ series. This is observed in molecular crystals because the d-d and d-sp interactions are weaker than in conventional divalent (and even monovalent) copper compounds. The decreasing exchange splitting is likely an additional factor affecting energy deepening of $3d$ states.

The deepening of d states across the series is accompanied by a shift towards higher binding energies of the maxima of the M $2p$ and M $3s$ XPS spectra of $M[N(CN)_2]_2$ in comparison with those for $3d$ monoxides.[24,25] This shift increases from about 0 eV for Mn$[N(CN)_2]_2$ to about 3 eV for Cu$[N(CN)_2]_2$. Due to weak metal-metal interactions in molecular crystals, especially in Cu$[N(CN)_2]_2$ where $3d$ states are strongly localized, the screening of the final states is weaker than in the other cases, resulting in larger binding energies of the valence bands and the core levels.

At the top of the valence band the detailed electronic structure is determined by the filling of the transition-metal $3d$ states. The local environment around M sites is a distorted octahedron of N sites, and the ligand field splits the $3d$ states by approximately 1.5 eV into t_{2g} and e_g manifolds. In Mn$[N(CN)_2]_2$, with an exchange splitting of over 3 eV, the majority d bands are fully occupied and there is a significant gap to the unoccupied minority d bands.[9] As the number of d electrons increases, the ligand-field splitting stays about the same while the exchange splitting decreases. The majority bands nevertheless remain filled. The minority t_{2g} bands are narrow and split by the tetragonal distortion of the local octahedral environment and by the longer-range crystal field. In the FM configuration, intersublattice d-d interactions broaden the majority t_{2g} bands, resulting in a twofold subband of $d_{xz,yz}$ states with a gap to the d_{xy} subband. (Axes are referenced to the local octahedral environment.) In the AF configuration, intersublattice d-d interactions are suppressed, which narrows the t_{2g} bands. For $M=$Fe, the ordering of the onefold and twofold subbands reverses in the FM phase. Thus, with one minority t_{2g} electron per Fe site, AF Fe$[N(CN)_2]_2$ is metallic while FM Fe$[N(CN)_2]_2$ is insulating, as shown in Fig. 11. The lack of a gap in AF Fe$[N(CN)_2]_2$ with collinear spins contributes to its instability with respect to the insulating FM phase. In FM Co$[N(CN)_2]_2$, the twofold subband fills, and in FM Ni$[N(CN)_2]_2$, the t_{2g} manifold is completely occupied. The Jahn-Teller effect significantly enhances the tetragonal distortion of the octahedral environment around Cu sites in Cu$[N(CN)_2]_2$,[4,5] which increases the splitting between e_g bands. The calculated GGA band gaps are listed in Table I, along with estimated gaps from diffuse reflectance spectroscopy. The agreement is better for the compounds where the t_{2g} band is either completely empty or completely full.

The narrow width of some of the d bands (Fig. 11) suggests that electron correlations could be important in these materials. Additional evidence for this is the GGA's large underestimation of the band gaps in some of the compounds, particularly Co$[N(CN)_2]_2$. Furthermore, the fact that the measured magnetic moments in Fe$[N(CN)_2]_2$ and Ni$[N(CN)_2]_2$ are larger than the maximum moments that

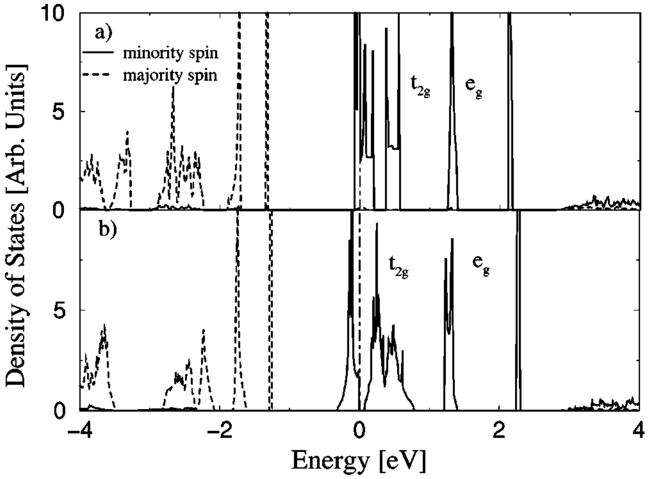

FIG. 11. Fe *d* density of states calculated for $\mathrm{Fe[N(CN)_2]_2}$ with (a) AF spin ordering and (b) FM spin ordering. The linear tetrahedron method is used to calculate the DOS.

could be created by spin alone indicates the importance of the orbital moment. Therefore methods incorporating orbital dependence of the potential could significantly improve the results. The situation is reminiscent of the monoxides of the 3*d* transition metals. As with the oxides, it is likely that methods beyond DFT-GGA are needed for a better description of the electronic and magnetic structure of the dicyanamides in the solid state.

V. CONCLUSIONS

We have carried out a theoretical and experimental investigation of the electronic structure of the $M\mathrm{[N(CN)_2]_2}$ ($M=\mathrm{Mn,Fe,Co,Ni,Cu}$) molecular magnets. The general features of the valence bands are similar across the series, with the primary exceptions being the location of the 3*d* bands with respect to the Fermi level and the degree of hybridization between M 3*d* states and N 2*p* states. Going across the row from Mn to Cu, the *d* bands lie deeper in energy, and the degree of hybridization with N *p* states increases.

Total-energy calculations indicate that the small differences in structural parameters (for example, the angle of the superexchange pathway) found in these isostructural materials is not sufficient to account for differences in their magnetic ground states. Rather, the occupation of the 3*d* shell is likely a more significant factor.

For most of the materials in the series, our calculations underestimate either the band gap or the local magnetic moment. Together with the existence of narrow *d*-bands in these materials, this suggests that a better description of the magnetic and electronic structure of these materials will require a more accurate treatment of electron-electron interactions.

ACKNOWLEDGMENTS

The authors thank M. R. Pederson for helpful discussions and for communicating unpublished results. V.R.G. acknowledges support from the Deutscher Akademischer Autstauschdienst (DAAD) Program. This work was supported by the Research Council of the President of the Russian Federation under Grant No. NSH-1026.2003.2, the Russian Foundation for Basic Research under Project No. 02-02-16674, the President's NSERC fund of the University of Saskatchewan, Deutsche Forschungsgemeinschaft (DFG) under the priority program SPP 1137 Molekularer Magnetismus, the U.S. National Science Foundation under Grant No. DMR-0210717, and the U.S. Office of Naval Research under Grant No. N00014-02-1-1046. Work at the Advanced Light Source at Lawrence Berkeley National Laboratory was supported by the U.S. Department of Energy under Contract No. DE-AC03-76SF00098. Work at the Advanced Photon Source is supported by the U.S. Department of Energy, Office of Science, Office of Basic Energy Sciences under Contract No. W-31-109-ENG-38.

---

*Present address: Paul Scherrer Institut, Swiss Light Source, CH-5232 Villigen, Switzerland.

[1] J.M. Manriquez, G.T. Yee, R.S. McLean, A.J. Epstein, and J.S. Miller, Science **252**, 1415 (1991).
[2] S. Ferlay, T. Mallah, R. Ouahes, P. Veillet, and M. Verdaguer, Nature (London) **378**, 701 (1995).
[3] J.L. Manson, C.R. Kmety, Q. Huang, J.W. Lynn, G.M. Bendele, S. Pagola, P.W. Stephens, L.M. Liable-Sands, A.L. Rheingold, A.J. Epstein, and J.S. Miller, Chem. Mater. **10**, 2552 (1998).
[4] S.R. Batten, P. Jensen, B. Moubaraki, K.S. Murray, and R. Robson, Chem. Commun. (Cambridge) **3**, 439 (1998).
[5] M. Kurmoo and C.J. Kepert, New J. Chem. **22**, 1515 (1998).
[6] C.R. Kmety, Q. Huang, J.W. Lynn, R.W. Erwin, J.L. Manson, S. McCall, J.E. Crow, K.L. Stevenson, J.S. Miller, and A.J. Epstein, Phys. Rev. B **62**, 5576 (2000).
[7] C.R. Kmety, J.L. Manson, Q. Huang, J.W. Lynn, R.W. Erwin, J.S. Miller, and A.J. Epstein, Phys. Rev. B **60**, 60 (1999).
[8] C.R. Kmety, Ph.D. thesis, The Ohio State University, 2000.
[9] M.R. Pederson, A.Y. Liu, T. Baruah, E.Z. Kurmaev, A. Moewes, S. Chiuzbǎian, M. Neumann, C.R. Kmety, K.L. Stevenson, and D. Ederer, Phys. Rev. B **66**, 014446 (2002).
[10] J.J. Jia, T.A. Callcott, J. Yurkas, A.W. Ellis, F.J. Himpsel, M.G. Samant, J. Stöhr, D.L. Ederer, J.A. Carlisle, E.A. Hudson, L.J. Terminello, D.K. Shuh, and R.C.C. Perera, Rev. Sci. Instrum. **66**, 1394 (1995).
[11] G. Beamson and D. Briggs, *High Resolution XPS of Organic Polymers: The Scienta ESCA300 Database* (Wiley, Chichester, 1992).
[12] G. Kresse and J. Furthmüller, Comput. Mater. Sci. **6**, 15 (1996); Phys. Rev. B **54**, 11 169 (1996).
[13] Y. Wang and J.P. Perdew, Phys. Rev. B **44**, 13 298 (1991).
[14] J.P. Perdew, K. Burke, and M. Ernzerhof, Phys. Rev. Lett. **77**, 3865 (1996).
[15] H.J. Monkhorst and J.D. Pack, Phys. Rev. B **13**, 5188 (1976).
[16] M.R. Pederson and T. Baruah, private communication.
[17] E. Ruiz, J. Solid State Chem. **176**, 400 (2003).
[18] P.W. Anderson, Phys. Rev. **79**, 350 (1950); **115**, 2 (1959).
[19] J.B. Goodenough, *Magnetism and the Chemical Bond* (Wiley, New York, 1963).
[20] H. Weihe, H.U. Güdel, and H. Toftlund, Inorg. Chem. **39**, 1351 (2000).

[21] B.N. Figgis, *Introduction to Ligand Fields* (Wiley, New York, 1966).

[22] J.H. Van Vleck, Phys. Rev. B **45**, 405 (1934).

[23] V.R. Galakhov, S. Uhlenbrock, S. Bartkowski, A.V. Postnikov, M. Neumann, L.D. Finkelstein, E.Z. Kurmaev, A.A. Samokhvalov, and L.I. Leonyuk, cond-mat/9903354 (unpublished).

[24] V.R. Galakhov, L.D. Finkelstein, D.A. Zatsepin, E.Z. Kurmaev, A.A. Samokhvalov, S.V. Naumov, G.K. Tatarinova, M. Demeter, S. Bartkowski, M. Neumann, and A. Moewes, Phys. Rev. B **62**, 4922 (2000).

[25] V.R. Galakhov, M. Demeter, S. Bartkowski, M. Neumann, N.A. Ovechkina, E.Z. Kurmaev, N.I. Lobachevskaya, Ya.M. Mukowskii, J. Mitchell, and D.L. Ederer, Phys. Rev. B **65**, 113102 (2002).

[26] C.R. Kmety, J.L. Manson, S. McCall, J.E. Crow, K.L. Stevenson, and A.J. Epstein, J. Magn. Magn. Mater. **248**, 52 (2002).